Morphology controlled synthesis, magnetic properties and electrochemical study of hematite nanocrystals

**A thesis submitted towards partial fulfillment of
BS-MS Dual Degree Programme**

IISER PUNE

By

SURYA R.
(BS-MS student, Registration No.: 20121074)

Under the guidance of

Dr. Seema Verma

Department of Chemistry
Indian Institute of Science Education and Research (IISER) Pune, India

Dedicated to my family, teachers and friends

Certificate

This is to certify that this dissertation entitled "**Morphology controlled synthesis, magnetic properties and electrochemical study of hematite nanocrystals**" towards the partial fulfillment of the BS-MS dual degree programme at the Indian Institute of Science Education and Research Pune, represents original research carried out by **Surya R** at IISER Pune under the supervision of "**Dr. Seema Verma**, Faculty Fellow, Department of Chemistry, IISER Pune" during the academic year of 2016-2017.

Seema Verma

Date: 20/3/2017

Place: Pune

Dr. Seema Verma

Faculty Fellow
Department of Chemistry
IISER Pune

Declaration

I hereby declare that the matter embodied in the report entitled "**Morphology controlled synthesis, magnetic properties and electrochemical study of hematite nanocrystals**" are the results of the investigations carried out by me at the Department of Chemistry, IISER Pune, under the supervision of **Dr. Seema Verma** and the same has not been submitted elsewhere for any other degree.

SURYA R.

Date: 20/03/2017

Place: Pune.

Acknowledgments

List of Tables

List of Illustrations

Abbreviations

DRS   **Diffuse reflectance spectroscopy**

FESEM   **Field emission scanning electron microscopy**

FTIR   **Fourier transform infrared spectroscopy**

JCPDS   **Joint Committee for Powder Diffraction Standards**

OER   **Oxygen evolution reaction**

ORR   **Oxygen reduction reaction**

PTFE   **Polytetrafluoroethylene**

UV-VIS   **Ultraviolet visible**

XRD   **X-ray diffraction**

RD   **Rotating Disc Electrode**

RRD   **Rotating Ring Disc Electrode**

Table of Contents

Abstract

Rational design of the non-noble, robust and low-cost functional oxygen evolution and oxygen reduction reaction (OER/ORR) electrocatalysts are greatly desired for fuel cells, rechargeable Zn-air batteries and water electrolyzers. Zinc-air battery is considered as an ideal device for energy storage and conversion because of its projected high energy density and the long driving range per charge. Herein by varying the synthetic parameters we observed an interesting phase and morphological transformations in iron oxide nanostructures with interfacial chemistry selectively tunable towards OER or ORR. For the synthesis of electrocatalysts, a facile one-step hydrothermal route was developed utilizing lysine as a stabilizing agent. This study reveals that hybrid β-FeOOH @ α-Fe$_2$O$_3$ mixed phase favored selective OER over selective ORR favored on α-Fe$_2$O$_3$ nanocubes. Rate of the electrochemical OER is amplified by 300 times in β-FeOOH @ α-Fe$_2$O$_3$ that in turn is found to be significantly higher than the additive rate of their decoupled counterparts, indicating possible synergistic effects in the mixed phase. Perhaps the β-FeOOH sites act as water adsorption sites with its oxidation selectively catalyzed by α-Fe$_2$O$_3$ under applied bias. Integration of these electrocatalysts with selective interfacial activity to the air electrode of Zn-air battery ultimately lead to a rechargeable metal-air battery in tri-electrode configurations with ~500 mV reduction in the charging voltage. To the best of our knowledge, rechargeable metal air battery by tuning the interfacial chemistry of iron oxide nanostructures has not been studied earlier. When the OER electrocatalyst was absent, the air cathode required higher overpotentials indicating the role of OER catalyst in increasing the voltage and the overall energy efficiency. Magnetic hysteresis measurement on selected samples display ferromagnetism with exceptionally high coercivity in the range of 3.3 to 5.3 kOe at room temperature confirming induced ferromagnetism with exceptionally high anisotropy. Apart from the search for the materials of higher anisotropy, the present work demonstrates a strategy towards developing low-cost and abundant functional electrocatalyst for new generation metal-air battery.

CHAPTER 1

1. INTRODUCTION

For last few decades nanoscience and nanotechnology have attracted much attention and importance in the field of research due to its potential application in the area of engineering, science and technology. However, developments in nanotechnology are strongly dependent on the ability to design and correlate the enhanced properties with the application. Although synthesis, characterization and application of nanomaterials have been widely reported, one of the key challenges remains in creating a specific shape, size and morphology of the nanocrystals for its unique properties that can be exploited for applications.

Hematite, α-Fe_2O_3, isostructural with the rhombohedral corundum α-Al_2O_3 is one of the most important and interesting iron oxides with n-type semiconducting properties. Due to its favorable optical band gap of ~ 2.2 eV, extraordinary chemical stability in an oxidative environment, abundance and low cost, it has been extensively applied in the area of photoelectrochemical splitting of water, pigments, gas sensors etc.[1, 2] However, short hole diffusion length (2-3 nm), short excitation lifetime (~10pS), poor charge carrier mobility etc. limits the efficiency of hematite alone as a photoelectrochemical catalyst.[3] Doping with other metals like Ti, Zn, Sn, Cd etc. is reported to be an effective way to improve the performance of hematite as a photoelectrochemical catalyst and that has been effectively applied towards the photochemical degradation of dyes like methylene blue for water purification.[4, 5,6,7]

With the depletion of fossil fuels and petroleum products, there is great demand to look for other resources for generating and storing green energy. Fuel cells are one among those promising alternative.[8] As the heart of the fuel cell is its electrocatalyst, there is an immediate requirement to look for potential material which can replace high cost noble metal Ir, Pt and Pt based alloy catalyst with low cost efficient electrocatalyst for carrying out energy conversion processes such as oxygen evolution reaction (OER) and oxygen reduction reaction (ORR). In this direction,

though, transition metal oxides have withdrawn some attention, designing electrocatalyst of comparable efficiency remains a challenge.

Present work is an attempt to design an alternative electrocatalyst and study the interesting variation in OER and ORR activities of different phases and morphology of the iron oxide. The synthetic protocols were modified in such a direction that we get functional materials with enhanced electroactive surface area. The effort in this direction not only help us in fundamental understanding of the basic electrochemical properties of the materials, it also give us an opportunity to exploit the interesting properties of different phases of iron oxide for device fabrication such as in zinc – air battery.

1.1. Oxygen evolution reaction (OER)

Oxygen evolution reaction is an important reaction involved in water splitting reaction and metal air batteries. OER consist of four-electron oxidation of two water molecules and removal of four protons to form oxygen-oxygen bond.[9]

In acidic condition reaction happen by oxidation of two water molecule to form four proton and formation of one oxygen molecule.

$$2H_2O \rightleftharpoons 4H^+ + O_2 + 4e^-$$

In basic condition the OH^- ions present will transform into H_2O molecule and O_2 molecule with the transfer of electrons.

$$4OH^- \rightleftharpoons 2H_2O + O_2 + 4e^-$$
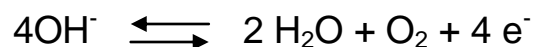
This multi electron transfer reaction is kinetically not favorable and requires large overpotential. Overpotential is the term which defines the difference between the experimental and thermodynamic potential. The thermodynamic potential for OER is 1.23V vs RHE at all pH. Thermodynamic potential give only minimum potential required for a process and experimentally the reaction happens at a higher voltage. Electrocatalysts are developed to make this reaction

happen at lower overpotential with high current density. An ideal electrocatalyst should have low overpotential, low cost, earth abundance and stability.

Several metals and metal derivatives show high catalytic activity towards OER. Noble metals, Ir and Ru and its compound (for example IrO_2 and RuO_2) are well studied OER catalyst which exhibit lower overpotential and high current density.[10, 11] However the high cost, scarcity and toxic effect of noble metals prevent the use of these materials in industrial scale.[12] Researchers are trying to develop non-noble metals or its derivatives having a better catalytic performance towards the oxygen evolution reaction. Because of the commercial importance of OER activity, efficiency of cost effective and earth abundant first row transition metal oxides such as Ni, MnO_2,[13] Co_3O_4[14] has been studied extensively. Nickel is most widely used electrocatalyst for OER and it shows low corrosion rate in alkaline media. Co based perovskites are used as OER catalyst as a substitute for noble metals and metal derivatives.[15] Graphene cobalt oxide nano composite also showed enhanced catalytic activity towards the oxygen evolution reaction in alkaline media.[16]

1.2. Oxygen reduction reaction (ORR)

Oxygen reduction reaction (OER) plays important role in determining the performance of fuel cells and rechargeable metal air battery. Platinum metal shows better catalytic activity towards ORR. The use of precious metal like platinum in the fuel cells limits the industrial scale production of devices. Moreover very large amount of platinum metal required for accelerating kinetically sluggish oxygen reduction reaction and it also have poor stability in alkaline media. Platinum alloys with non-precious metals like Ni, Co and Fe shows enhanced ORR activity and this approach reduces the amount of platinum usage.[17] For last few years, researchers are developing less expensive and more abundant non-noble metal based catalyst for the oxygen reduction reaction. Transition metals (Cu, Ti etc) metal oxides and metal alloys have been investigated for electrocatalytic ORR activity.[18] Composite material of iron oxide nano particle with carbon nanotube, graphene etc has been investigated recently for the ORR catalytic activity.[19, 20]

1.3 Zinc Air Battery

Metal air battery shows high energy density compared to other rechargeable batteries.[21] These batteries are more appropriate for the vehicular propulsion since it uses oxygen from air as a cathode material. The anode of metal air battery is made up of pure metals such as Al, Ge, Ca, Fe, Li etc. Among these metal air batteries zinc-air battery attract more attention because of its electropositive character and stability in aqueous and alkaline media without significant corrosion.[22]

1.3.1 Working of zinc air battery

As shown in the Figure 1.1 in a typical zinc air battery consist of zinc electrode, a membrane separator and porous air electrode assembled together in alkaline media. Zinc act as a negative electrode (anode) and the porous air electrode act as a positive electrode (cathode).

Figure1.1: Schematic of a zinc air battery[23]
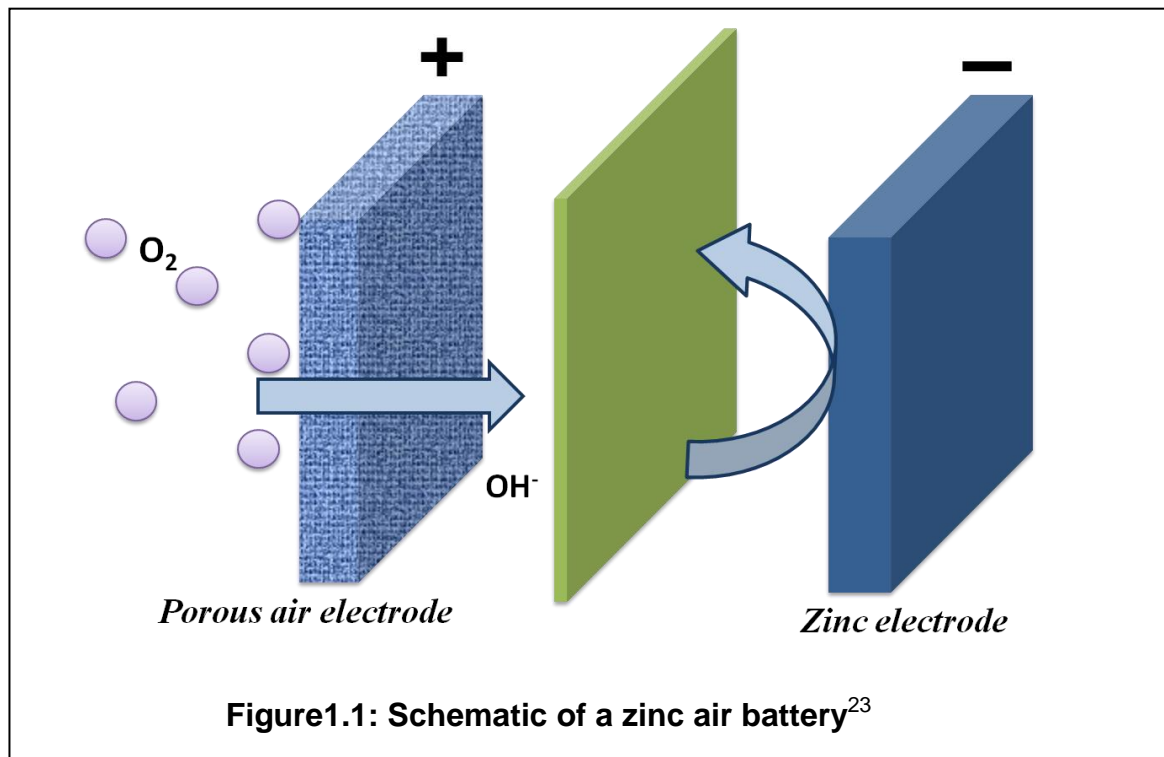
During discharge, oxidation of zinc occurs and it gets converted to soluble zincate ions ($Zn(OH)_4^{2-}$). After the saturation of this conversion zincate will decompose to zinc oxide (ZnO). On positive electrode the O_2 from air will reduce (ORR) to form OH^-. A parasitic reaction between Zn metal and water will happen at negative and this unnecessary reaction will cause the corrosion of zinc electrode and reduce the efficiency of the device.

$$\text{Negative electrode:} \quad Zn + 4OH^- \longrightarrow Zn(OH)_4^{2-} + 2e^-$$

$$Zn(OH)_4^{2-} \longrightarrow ZnO + H_2O + 2OH^-$$

$$\text{Positive electrode:} \quad O_2 + 4e^- + 2H_2O \longrightarrow 4OH^-$$

$$\text{Overall reaction:} \quad 2Zn + O_2 \longrightarrow 2ZnO$$

$$\text{Parasitic reaction:} \quad Zn + 2H_2O \longrightarrow Zn(OH_2) + H_2$$
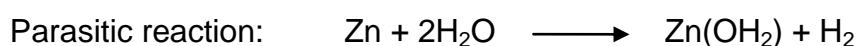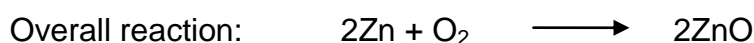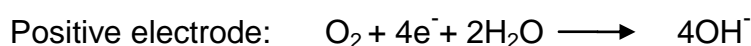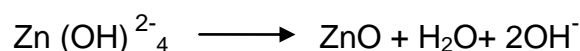
For rechargeable zinc air battery above process should reverse so that zinc will get deposited on negative electrode and oxygen will evolve at positive electrode. Upon recharge the reluctance of zincate to go back to initial state reduce the efficiency of zinc air battery. Several bifuctional catalysts are used for zinc-air battery to catalyze both ORR and OER. Other important things that limit the efficiency of the metal air battery are the slow oxygen kinetics involved in oxygen electrochemistry and high over potential associated with these two reactions.[24] Scarcity and cost will hinder the large scale production of precious metal for metal air battery. Therefore, it is important to develop, efficient, stable and affordable catalyst for OER as well as ORR for zinc - air battery.

1.4. Synthesis of Fe_2O_3 nanostructures

Morphology controlled synthesis of nanocrystalline materials are of great interest and are actively being pursued as morphology of materials strongly governs their performance. In the literature, several methods are available for the synthesis of hematite nanoparticles of different morphologies such as nanospheres, nanorods, nanobelts, nanowires, nanocubes, nanoflowers etc. by several solution based methods. [25,26,27,28] However, most of these synthetic routes requires

presence of organic surfactants, alkali ions, templates, calcination etc. and often the synthesis protocols requires different stabilizing agents like fluoride, phosphates, chlorides etc. for tailoring the morphologies making the protocol tedious and time-consuming.[29,30] In the present investigation we report a convenient hydrothermal route utilizing Lysine as a hydrolyzing and stabilizing agent and found that an interplay between concentration of Fe salts and Lysine largely governs the morphology of iron oxides. We were able to synthesize large scale, monodispersed hematite nanocubes and akaganeite nanorods by the same synthetic route without using any additional surfactant or template. Lysine not only acted as a good hydrolyzing controlling agent but also helped in maintaining the pH of the solution.

1.5. Magnetic Properties of α-Fe$_2$O$_3$

Hematite is known to show antiferromagnetism owing to the superexchange interactions between the Fe spins in adjacent layers, mediated by oxygen ions. However, when hematite is prepared in nanoparticle form, the broken exchange interactions and reduced coordination especially on the surface of the nanoparticles results uncompensated spins. This leads to the significant enhancement in the magnetization due to induced ferromagnetism. Therefore, it is interesting to study the effect of the size and shape of the nanocrystals on magnetic properties.

CHAPTER II

2. Materials and methods

This chapter discusses about the synthetic protocols and different reaction conditions adopted for the synthesis of hematite nanoparticles of varying morphologies, shapes and sizes. Details about the fabrication of electrode for electrocatalytic study are discussed. A brief background of analytical techniques used for the characterization of the samples such as X-ray diffraction (XRD), field emission scanning electron microscopy (FESEM), Fourier transform infrared (FTIR) spectroscopy and thermogravimetric analysis (TGA), SQUID magnetometer and UV-Vis spectroscopy is also discussed.

2.1. Hydrothermal synthesis of Hematite nanoparticles

It is very important to develop a synthetic route in order to obtain nano materials with desired physical and chemical properties, narrow size distribution, shape and pure crystalline phase. Nano particles possess high surface energy due to the large surface to volume ratio, and consequently particles aggregates to reduce the excess surface energy. It is very important to maintain the size and shape of nano particles for desired properties and its application. Though, coating nanoparticles with organic, inorganic or any other polymer molecules prevents the aggregation, presence of surfactants and templates sometimes limits the application and the productivity scale. Here in this present work we synthesized hematite nanocubes by one - step hydrothermal synthesis without any surfactants or external template. Hydrothermal synthesis consists of the formation of nucleation site under high temperature and pressure. In hydrothermal method substance undergo crystallization inside a sealed container at a high temperature (120^oC to 250^oC) and at high vapor pressure ensuring better crystallinity of the product.

2.1.1. Experimental section

L- Lysine monohydrochloride (2g) was added to the 30 ml solution of $FeCl_3.6H_2O$ (1.3g) in the 2:1 molar ratio and were mixed well to obtain a homogeneous solution. Then the solution was transferred to 50 ml of teflon lined autoclave. Sealed autoclave was kept inside the 180^oC preheated oven for 12 hrs. After the reaction the autoclave was cooled down to room temperature naturally. Several experiments were conducted by adjusting the temperature, hydrothermal reaction time and aging time in order to study the growth mechanism and optimizing the condition for desired product. The metal to lysine ratio was changed in systematic way to demonstrate the effect of this ratio on final product. We could able to change the size of the hematite nanoparticles by altering the metal to lysine ratio. After synthesis, the product was obtained by centrifugation and washing with water and ethanol for several time. And finally the last product dried at 80^oC in an oven.

2.2. Electrode preparation for OER and ORR study

Electrochemical measurements were performed in a solution of 1M KOH using three electrode cell. Platinum foil and Hg/HgO electrodes were used as counter and reference electrode respectively. The slurry of sample was prepared by dispersing active material, activated charcoal and poly (tetrafluro-ethylene) (PTFE) in the mass ratio of 80:15:5. The resulting mixture was ultrasonicated for 30 minutes. OER and ORR of the catalyst were studied using Rotating Disc Electrode (RDE). 5µl of slurry was drop casted onto the glassy carbon electrode having diameter 5mm. 1 M KOH was used as the electrolyte and all measurement were taken at 1600 rpm. The solution was saturated with oxygen prior to the experiment.

2.2.1. Calculation of Collection efficiency and Faradic Efficiency

Faradic efficiency O_2 production of catalyst was measured using Rotating Ring Disc Electrode (RRDE). Collection efficiency was calculated for the catalyst by reducing $K_3Fe(CN)_6$ at glassy carbon disc electrode and re oxidizing at the platinum ring. RRDE measurements were conducted by purging N_2 gas for 10- 15 minutes and ensured the surface purging during

experiment. Electrodes were prepared prior to the measurement by drop casting the catalytic material on the 5 mm glassy carbon disc. Disc electrode was subjected to 2 minute current step at different currents while the ring was held at 0.7 V vs Hg/HgO. And the experiment was conducted in 1MKOH at 1600 rpm.

2.3. Electrocatalyst preparation and fabrication of zinc air battery

A homogeneous mixture of catalytic coating material was made by mixing electrocatalyst with 10% super P carbon and 10% of PTFE binder. The resulting mixture was ultrasonicated for 30 minutes to form slurry. OER and ORR catalytic mixture was coated onto a carbon cloth with loading 3mg/cm^2 rate.

Zinc-O$_2$ battery was fabricated in a closed electrochemical cell with tri-electrode configuration with Zinc foil as anode, ORR cathode catalyst and OER cathode catalyst. And the humidified O$_2$ was supplied to the cell. Electrochemical evaluation of the battery was performed using Biologic VMP 300.
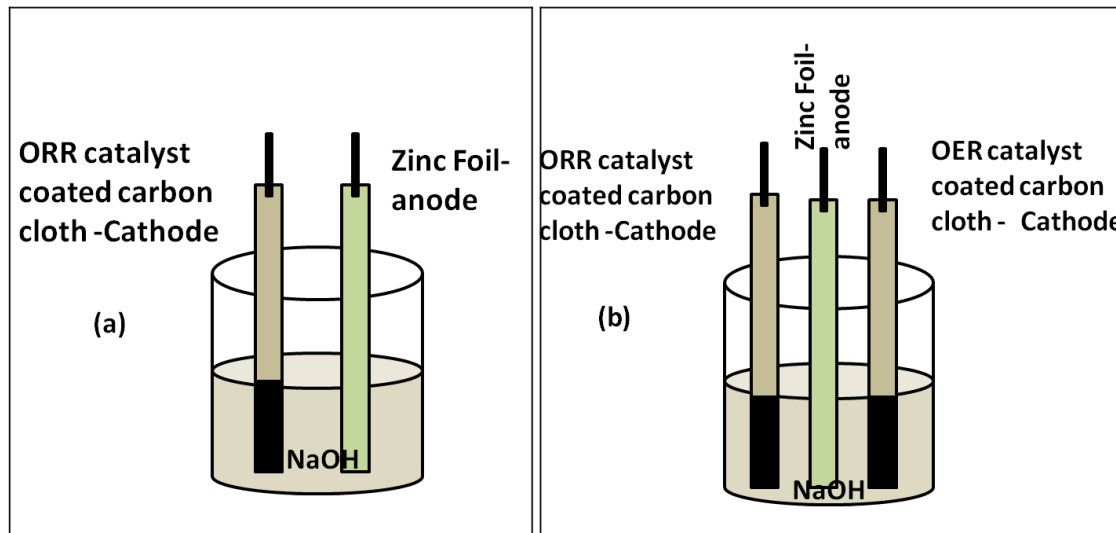

Figure 2.1: Schematics for electrochemical cells for measurements of primary (a) and rechargeable (b) Zn-air batteries.[23]

2.4. Material characterization technique

This section provides a brief background of structural characterization technique, used for the identification of crystallographic structure, morphology etc. of nanostructures and spectroscopic techniques, which is necessary to understand the optical and chemical nature of nanoparticles.

2.4.1. X-ray diffraction

X-ray diffraction technique (XRD) is commonly used for the determination of crystal structure, grain size, lattice parameter, strains, defects etc. X-rays, which is a part of electromagnetic spectrum with a wavelength 0.5 - 2.5 Å, are used in XRD technique. Diffraction occurs when monochromatic X-Rays interact with electron cloud of regularly arranged atoms in a crystal. The incident X-ray scattered in all directions. However, at certain angle (θ) the incident light and scattered light remain in phase and this is the condition for constructive interference.

Diffraction of X-rays by the periodically arranged atoms in the crystal depends on the angle of incident beam and the orientation of atoms (h, k, l values). Bragg's law gives the condition for constructive interference of scattered light.[31]

$$2d\ sin\theta = n\lambda$$

Where d is the distance between two crystal planes, θ is the angle between incident beam and transmitted wave and λ is wavelength of X- ray.
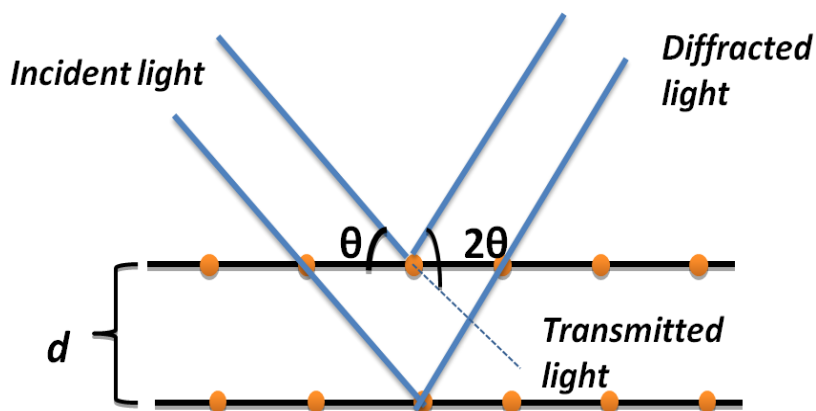
Figure 2.2: Schematis diagram of conditios for braggs law

Samples were evaluated by plotting the intensities as a function of angular position (2θ) values and this plot represent the characteristic diffraction pattern of each material.In the current project phase purity and crystalline structure were investigated by powder XRD using the a model D8 ADVANCE BRUKER diffract meter at IISER Pune equipped with Ni-filtered CuKα radiation source (λ = 1.5418 Å, 40 kV and 30 mA).

2.4.2. Scanning electron microscopy

Field emission scanning electron microscopy (FESEM) gives the information of morphology of the material by providing high magnification images using electron beam. Compared to scanning electron microscopy (SEM), FESEM provides clearer, less distorted images with more spatial resolution. In FESEM, electron beams are generated by the field emission source (FES) which generates electrons by applying high electric potential gradient to a tungsten wire with sharp tip(radius ∼ 100nm). These electrons will interact with sample and produce secondary electrons.

Secondary electrons ejected from the sample contain the information of the surface structure of the material.

2.4.3. Fourier Transform Infrared Spectroscopy

Infrared region of electromagnetic spectrum is used in IR spectroscopy for the identification of chemical bonding in the material. A molecule has many vibrational modes but only few are considered as IR active. A vibrational mode which is associated with change in permanent electric dipole moment is considered as IR active and this will appear in IR spectrum. A characteristic IR spectrum, a plot of transmittance or absorbance as a function of wave number, gives the information about the chemical bond in the sample. The pellets for the IR measurement were prepared by mixing synthesized iron oxide samples with KBr (sigma Aldrich, FTIR spectroscopy grade). The FTIR measurement of these samples was carried out on a Nicolet 6700 FTIR spectrometer at IISER Pune, INDIA.

2.4.4. UV-Vis spectroscopy

When an electromagnetic radiation with a wavelength in the range of 200-800nm (UV-VIS) interact with substance, a characteristic portion of the wavelength is absorbed. Other portion of the radiation either transmitted or reflected by the substance. Absorbed wavelength is used for the electronic transition in the molecules.[32] Absorbance is directly proportional to the concentration of the absorbing species **C** and path length **l.** And the relation is given by Beer Lamberts law

$$A = \varepsilon c l$$

Where **ε** is the molar absorption coefficient.
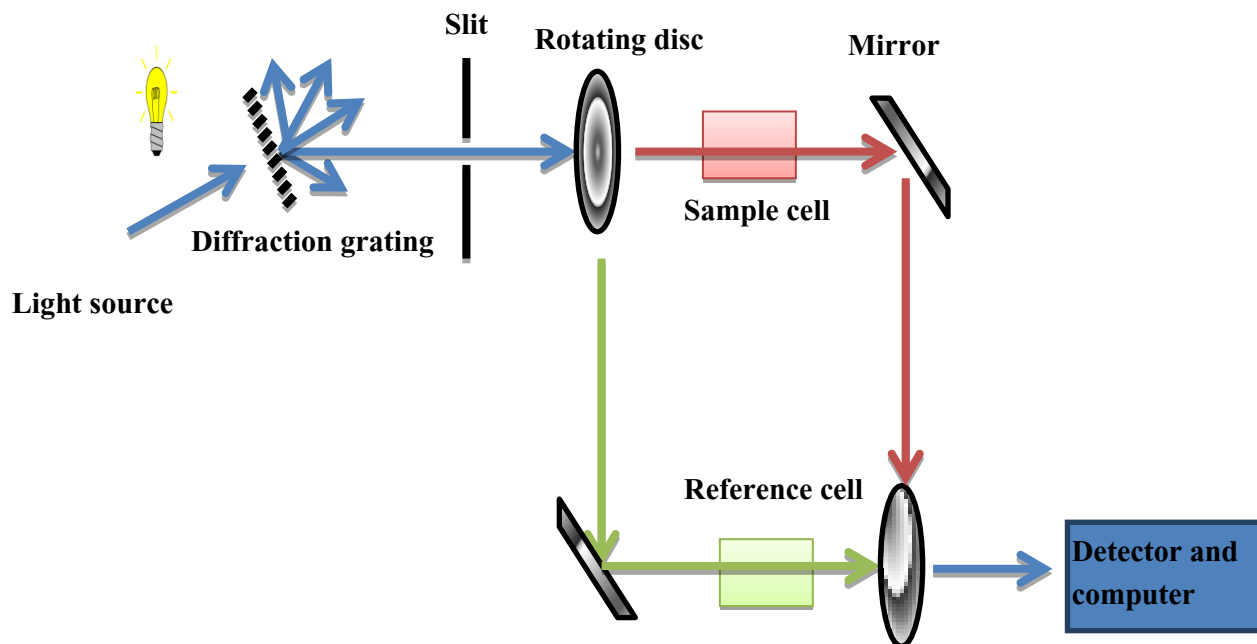
Figure 2.3: Schematic of transmission mode UV-Vis spectroscopy[33]

Transmission mode of optical measurement is not suitable for opaque thin films and particles that are not well dispersed in any solvents since it does not transmit the incident light. Diffuse reflectance spectroscopy is useful for this sample, which measures the reflectance after absorption of incident light. UV-Vis diffuse reflectance spectroscopy (DRS) was carried out by means of a model 2100 UV-Vis Shimadzu spectrophotometer equipped with a diffuse reflectance attachment and a data acquisition system. Spectra were taken, over the wavelength range 200-1200 nm, circular compacts of test materials against a $BaSO_4$ compact (a product of Shimadzu Corp.) used as a totally reflective reference material.

CHAPTER III

3. Results and discussion

3.1. Synthesis of hematite nanostructures

In the present investigation, we report a simple hydrothermal method to synthesize iron oxyhydroxide phase akaganeite (β-FeOOH) nanorods which undergo morphological and nanostructural phase transformation to α-Fe_2O_3 nanocubes. The growth of hematite subsequent to akaganeite precipitation can be rationalized based on their dissolution and recrystallization process at equilibrium. To confirm the reaction intermediates and formation mechanism of nanocrystals a systematic time dependence experiments were conducted. This has allowed us to systematically control the shape, sizes and morphologies of the nanocrystals simply by changing the hydrothermal conditions without changing the initial reagents. It is however expected that the shape, size, morphology and the rate of formation of hematite nanocrystals via the intermediate akaganeite phase should be largely dependent upon the kinetics of the first step leading to the nucleation of oxyhydroxide phase. To further explain the growth mechanism and the nature of hematite nanocrystals obtained, we examined effect of hydrothermal duration, temperature, digestion time, amino acid and concentration of the iron salt.

.

3.1.1. Effect of Hydrothermal Duration

In order to understand the intermediate and final phase formation, the products were obtained at different hydrothermal reaction time 2hrs, 8hrs, 10hrs, 12hrs and 48 hrs. The phase purity, phase transition and crystallinity of the nanocrystals were studied by XRD patterns. Figure 1 shows the XRD patterns of the samples obtained after reactions for different hydrothermal durations. It can be clearly seen that for 2hrs treated samples, the XRD peak positions and relative intensity of all the diffraction peaks matches well with tetragonal akaganeite phase (JCPDS 34-1266). It was found that as the hydrothermal reaction time progresses from 2 hrs to 8hrs, additional reflection corresponding to rhombohedral hematite phase was observed (JCPDS 86-0550). It is worth noting

that the XRD patterns of both the phases (see left Figure 3.1 B) are clearly confirming the occurrence of phase transition. With further increase in the hydrothermal duration from 8hrs to 10 hrs, the akaganite (β-FeOOH) phase undergoes complete phase transition to hematite phase (see left Figure 3.1 C and D). This clearly indicated that the formation mechanism of hematite nanocrystals may proceed via two steps: (i) hydrolysis of $[Fe(H_2O)_6]^{3+}$ to precipitate β-FeOOH phase under acidic conditions (ii) topotactic transformation of akaganeite to the hematite phase via the dissolution / reprecipitation mechanism.
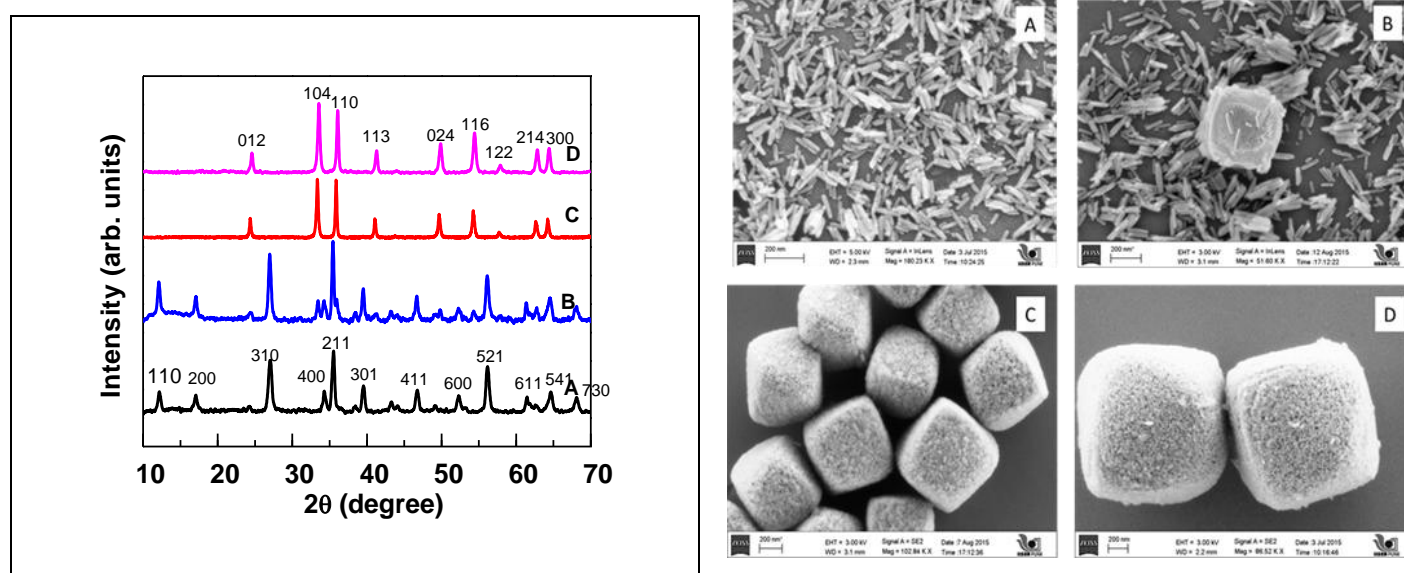
Figure 3.1: XRD patterns (left) and corresponding FESEM images (right) of samples obtained from hydrothermal treatment time of (A) 2 hrs, (B) 8 hrs, (C) 10 hrs, (D) 12 hrs

It has been earlier reported that the formation of akaganeite phase is favored by the presence of Chloride ions (Cl⁻) under acidic condition.[34]The formation mechanism of Hematite is represented by the following steps:

$$Fe^{3+} + 2H_2O \rightarrow FeO(OH) + 3H^+ \qquad (1)$$
$$Fe^{3+} + 3H_2O \rightarrow Fe(OH)_3 + 3H^+ \qquad (2)$$
$$2\,Fe(OH)_3 \rightarrow Fe_2O_3 + 3H_2O \qquad (3)$$
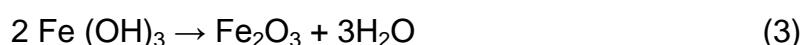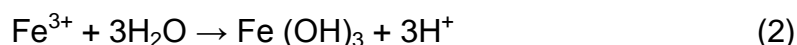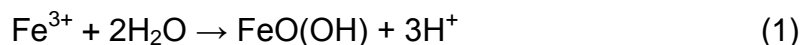
An analysis of the FESEM images clearly indicated the initial formation of highly mono dispersed β-FeOOH nanorods which self-assembles and simultaneously undergoes phase transformation to α-Fe$_2$O$_3$ nanocubes. The size of the nanotubes was found to be of diameter 30 (± 10) nm and length 90 (± 10) nm. The nano tubes were found to undergo self-assembly to form nano cubes of sizes ranging from 600 - 700 nm, which undergoes increase in their dimension with the increase in the treatment time

3.1.2. Role of reaction temperature on growth of α-Fe$_2$O$_3$

To gain more information about the evolution of hematite nanocubes, effect of reaction temperature has been studied by conducting experiment at 140°C, 180°C and 200°C by keeping all other reaction parameters constant. An analysis of XRD and corresponding FESEM images (see Figure 3.2) clearly indicated that β-FeOOH to α-Fe$_2$O$_3$ phase and morphological transition requires an optimum temperature and the phase transition happen with the evolution of large amount of gases. This can be manifested from the fact that 140°C treated sample remains at initial β-FeOOH phase (JCPDS 34-1266) even after 10 hrs of treatment (see Figure 3.2 a & b) whereas for 200°C treated samples both phase as well as morphological transitions happens simultaneously at initial 2hrs of treatment (see Figure 3.2 e). This may be attributed to the favored conditions at 200°C due to increased kinetics and decreased activation energy facilitating the self-assembly of nanotubes to nanocubes. It is interesting to note that at higher temperature (200°C) the nanocubes obtained were much more porous and this might be attributed to the evolution of large amount of gases due to breaking of lysine and simultaneous phase transition from β-FeOOH to α-Fe$_2$O$_3$ phase.
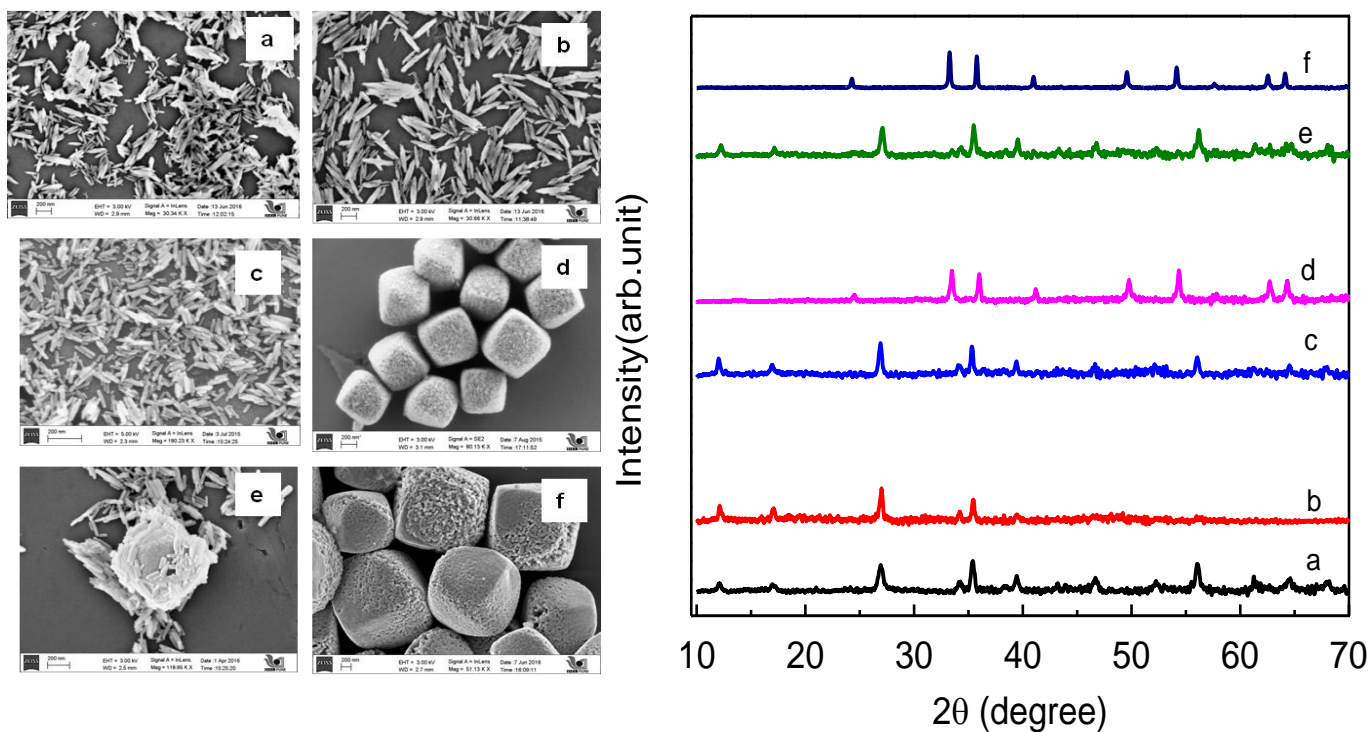
Figure 3.2: FESEM image and corresponding XRD patterns of 140 ˚C, 180 ˚C and 200°C heat treated samples for the duration of 2hrs (a, c, e) and 10hrs (b, d, f) respectively

3.1.3. Effect of salt concentration

We have successfully tailored the shape, size and morphological transition of the hematite nanocrystals with the systematic change in the iron salt concentration simply by changing the supersaturation level of the reaction mixture under the identical hydrothermal conditions. The detailed conditions for preparing some typical shape of the nanoparticles are mentioned in Table 1.

Table 1. Reaction conditions for obtained hematite nanocrystals

Sample	FeCl$_3$ conc. (M)	Duration(hrs)	Temperature(˚C)	Size(nm)	Morphology
1	0.0025 M	10	180	140	Spindle
2	0.005M	10	180	90	Ellipse
3	0.025M	10	180	100	Cubes
4	0.075M	10	180	200-500	Cube+Sphere

As illustrated from FESEM images (see Figure 3.3) the shape of the samples largely depends upon the concentration of iron salt and the shapes evolves from nanospindles, ellipsoidal, pseudocubes to perfect cubes. Concerning the morphological evolution of the α-Fe_2O_3 phase due to forced hydrolysis, the presence of iron ions and the chloride ions must play a key role, because all other reaction conditions are fixed for the samples. Indeed much work in this direction is required to elucidate this.
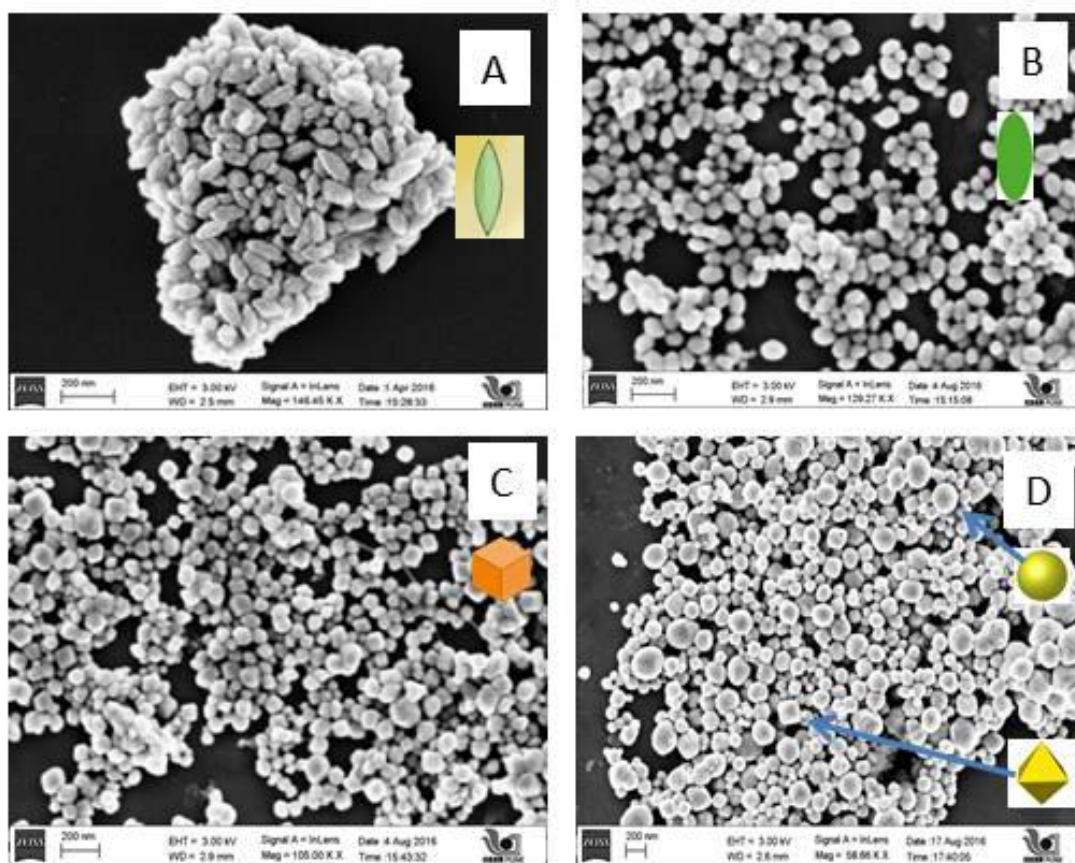

Figure 3.3: FESEM Images of the sample synthesized at lower supersaturation levels of Fe^{3+} ion (A)0.0025M, (B)0.005M, (C)0.025M and (D)0.075M

3.2. Magnetic measurement

Iron oxide nanoparticles were studied for their unique magnetic behavior. Field dependent magnetic behavior of the nanocrystals obtained at different hydrothermal treatment time is shown in the Figure 3.4 (a). The magnetization curve clearly shows that β-FeOOH phase is paramagnetic in nature whereas broad hysteresis loops with coercivity of ~3.5kOe confirms the presence of ferromagnetism in hematite α-Fe$_2$O$_3$ nanocubes of size ~1200 nm. Field dependent magnetic behavior of the nanocubes of sizes ranging from 1160 nm to 1260 nm, obtained at different hydrothermal conditions is shown in the Figure 3.4(b). It is interesting to observe broad hysteresis loop with coercivity values ranging from ~3.5 kOe to 5.3 kOe for particles of similar sizes. This confirms the presence of induced ferromagnetism with exceptionally high anisotropy. Though, the additional anisotropy is apparent from the shape anisotropy and not due to size variation, much work in this direction is required to elucidate the origin of high coercivity.
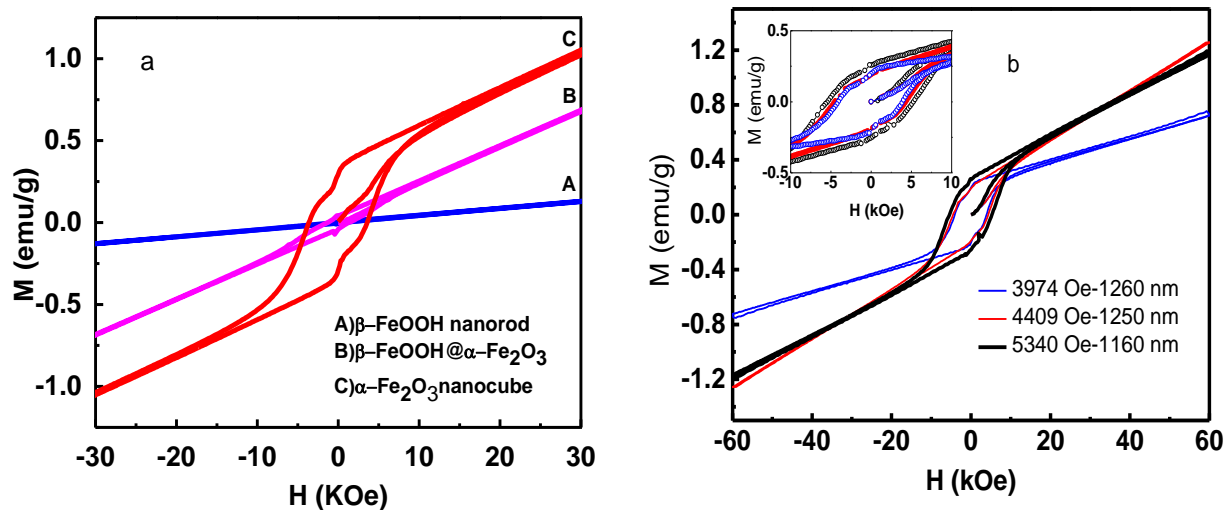

Figure 3.4: Field dependent magnetic properties of nanocrystals obtained after (A) 2hrs, (B) 8hrs and (C) 10 hrs hydrothermal treatments (a) Field dependent magnetization of hematite nanocubes of different sizes (a)

3.3. Optical property measurement

Optical absorption property of hydrothermally synthesized (at 180°C) α-Fe_2O_3 nano cube, β-FeOOH nanorods and α-Fe_2O_3@β-FeOOH hybrid were studied using diffuse reflectance solid state spectroscopy(DRS) in 300 -1200nm wavelength range as shown in figure3.5. It was well established that the electronic spectrum in Fe^{3+} in mainly due to three type of transitions that is Fe^{3+} ligand field transitions or the d-d transitions, the ligand to metal charge-transfer transitions, and the pair excitations resulting from the simultaneous excitation of two neighboring Fe^{3+} cations that are magnetically coupled.[35]
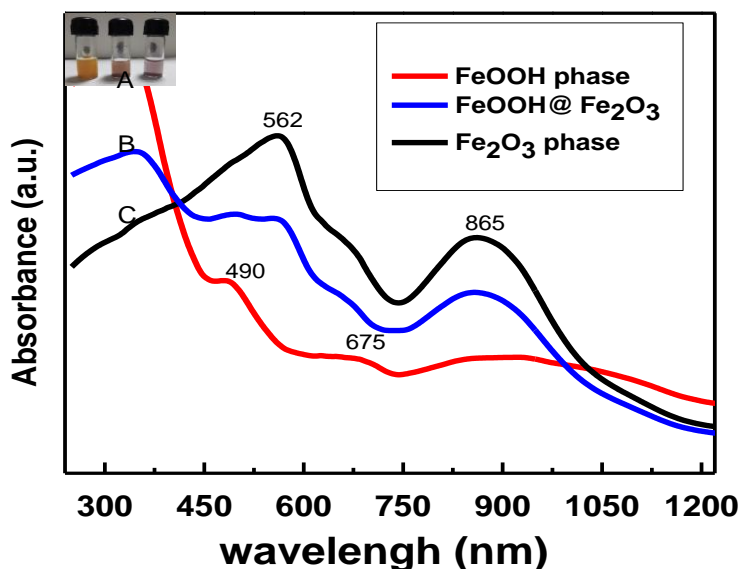
Figure 3.5: Diffuse reflectance spectra of α-Fe_2O_3 nanocube, β-FeOOH nanorods and
α-Fe_2O3@β-FeOOH hybrid phase

The absorption band of β-FeOOH (figure 3.5) mainly located in the 280-340nm range, and this is attributed to the Fe^{3+} ligand field transitions from $^6A_1$ to $^4T_1$. The 10 hrs sample (α-Fe_2O_3) shows two intense absorption bands, one is around 560nm and other around 860nm. As expected all three peaks are observed for the β-FeOOH@ α-Fe_2O_3 hybrid phase.

3.4.1. Catalytic activity towards Oxygen evolution reaction

OER activity was measured using rotating disc electrode at 1600 rpm and scan rate of 0.05 V/s. This low scan rate is sufficient enough to ensure the slow kinetics at electrode surface. The rotation rate (1600rpm) is enough to remove the species formed during the electrochemical reaction and thereby limit the formation of bubble at the electrode surface. The experiment conducted in 1M KOH and platinum and Hg/HgO electrodes were used as counter and reference electrode respectively.
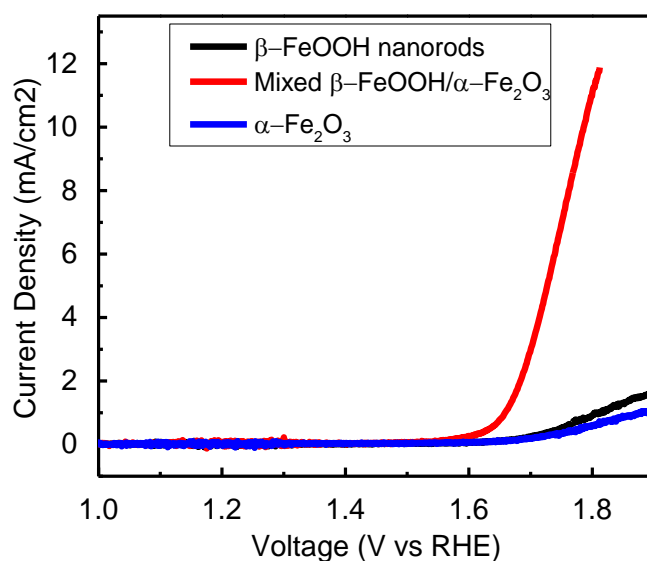
Figure 3.6: Linear sweep voltametry of the samples in O$_2$ saturated 1M KOH solution at a scan rate of 5mV/s and 1600 rpm.

The comparative OER catalytic performance of β-FeOOH nanorods,β-FeOOH@α-Fe$_2$O$_3$ phase and pure α-Fe$_2$O$_3$ nanocube is shown in the figure 3.6. The relevant figure of merit is the over potential required to achieve 10mA/cm^2 current density per geometric area at ambient temperature and 1atm O$_2$. This is approximately the current density expected at the anode in a

10%efficient solar water splitting devise under 1 sun illumination. [36, 37] The β-FeOOH @ α-Fe$_2$O$_3$ phase could able to achieve 10mA/cm^2 current density at the potential of 1.78V vs. RHE. Other two samples were less active compared to the β-FeOOH@α-Fe$_2$O$_3$ phase and it becomes saturated after 1.8V. This gives the clear evidence of enhanced electro catalytic activity of phase containing both β-FeOOH nanorods and α-Fe$_2$O$_3$ nanocubes. Other two samples fail to achieve the two important necessary conditions of OER catalyst, lower over potential and high current density.

In order to find the intrinsic activity of each sample it is important to normalize the rate of the catalytic reaction (current) with respect to the electrochemically active surface area. The actual electrochemical active area for each sample was calculated from double-layer capacitance of the catalytic electrode/electrolyte interface. The value of capacitance between 0V and 0.01V vs. Hg/HgO was used for the analysis. Double layer current was measured from cyclic voltametry at different scan rate for each sample. The product of scan rate (v) and electrochemical double layer capacitance(C) provide the double- layer charging current (i) and it is given by the equation;

$$i = Cv$$

The plot of double layer current as a function of scan rate will give a linear plot with a slope equal to the double layer capacitance of the electrode. Taking the capacitance of the flat electrode as 60μF/cm^2 the electrochemical surface area of the respective electrodes was calculated. The calculated electrochemical active area (A) of three different catalysts is listed in the Table 2.

Table 2. Electrochemically active surface area of catalysts.

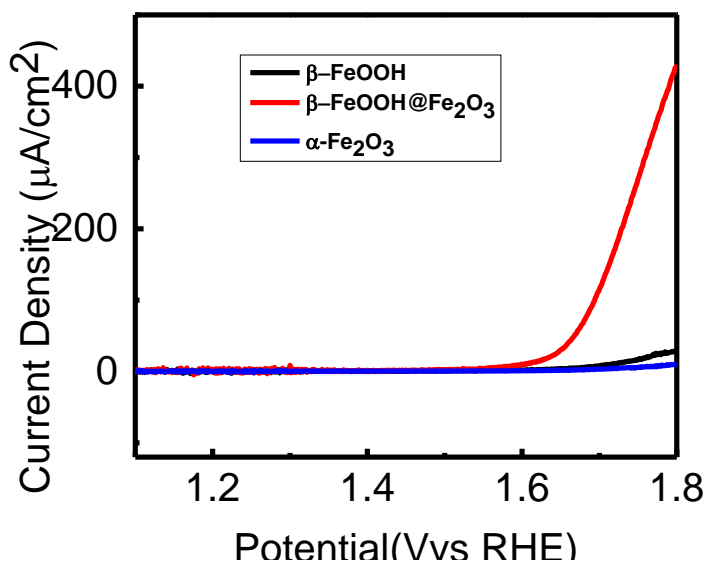| Catalyst	β-FeOOH nano rod	β-FeOOH @ α-Fe$_2$O$_3$	α-Fe$_2$O$_3$ nano cube
Area(cm^2)	6	5.05	11.65

Figure 3.7: Oxygen evolution current per true electrochemical surface area (current density) as a function of applied potential.

True area normalized oxygen evolution (OER) current was significantly amplified in the case of β-FeOOH@Fe$_2$O$_3$ by more than 300 times compared to other phases clearly revealing the intrinsic activity of the mixed phase towards the OER reaction. Since the rates on β-FeOOH@Fe$_2$O$_3$ are not an additive quantity of the individual rates on β-FeOOH and α-Fe$_2$O$_3$ phases, a synergistic effect is evidently present. Perhaps the β-FeOOH sites act as water adsorption sites and α-Fe$_2$O$_3$ phase selectively catalyzing the oxidation of water under applied bias. Their individual counterparts may be performing only one of the functions (either adsorptions or oxidation) and their proximity in β-FeOOH@Fe$_2$O$_3$ may be assisting each other. However this is a possible mechanism and further studies have to be carried out to understand it further.

Calculation of faradic efficiency (α-Fe$_2$O$_3$@β-FeOOH OER catalyst)

Rotating ring disc electrode (RRDE) apparatus helps to confirm the formation of oxygen formed during OER. The O$_2$ molecule formed at the disc electrode will be collected by the platinum ring electrode which is held at the reduction potential of O$_2$ (0.7V vs. Hg/HgO). The solution was purged with N$_2$ for 10 minute prior to the experiment in order to avoid the participation of dissolved oxygen in the experiment. The disc electrode was subjected to different current like 1mA/cm^2, 1.5mA/cm^2 and 5mA/cm^2 for a minute and the Faradaic efficiency was calculated based on the following equation.

$$\varepsilon = 2i_r / i_d N$$

Where *I$_r$* and *i$_d$* are ring and disc current respectively and *N* is the collection efficiency.

The change in potential as a function of elapsed time at constant current (chronopotentiometry) at the disc is shown in Figure 3.8(a). The O$_2$ generated at the disc electrode is swept towards the platinum ring electrode which is held at a constant potential (reduction potential of O$_2$), of 0.7 V vs Hg/HgO. Plot of current generated at the ring vs. time (chronoamperometry), held at 0.7V vs HG/HgO constant potential is shown in the Figure 3.8(b). Current generated at the ring electrode confirms the generation of oxygen at the disc electrode by catalytic activity of β-FeOOH@Fe$_2$O$_3$. Faradaic efficiency was calculated by measuring the individual ring current and disk currents. The Faradaic efficiency at 1mA/cm^2 is close to 100% however at higher currents the values were decreased to 63%.1mA/cm^2 is sufficiently large to ensure appreciable O$_2$ production but sufficiently small to minimize local saturation and bubble formation at the disk electrode.[38] Higher currents at the disk may generate large number of bubble and some of them could escape to the electrochemical cell before reaching the ring.
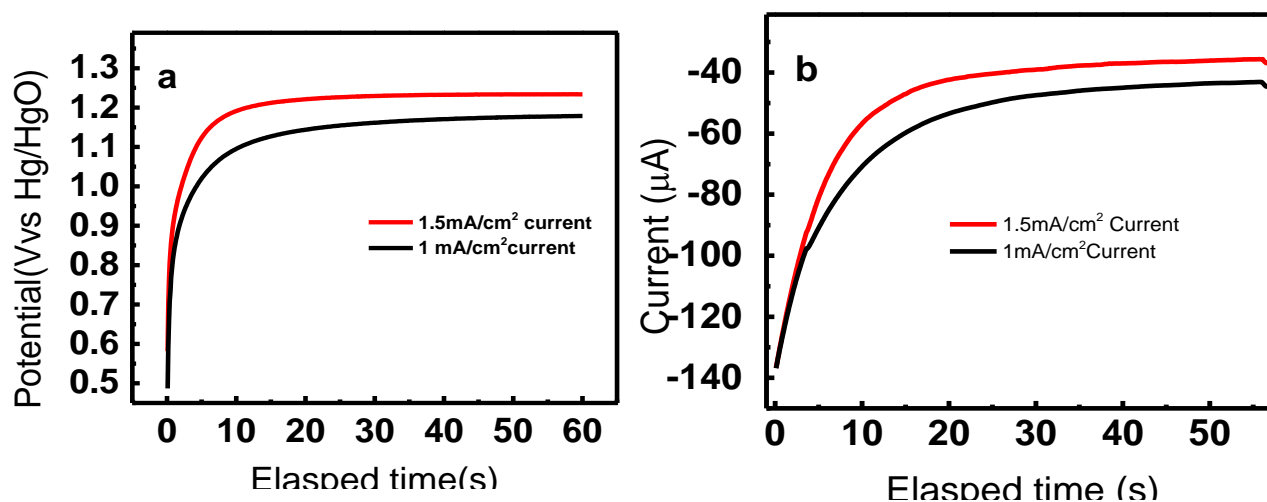
Figure3.8: (a) Chronopotentiometry plot for the disc electrode at different currents (b) Corresponding chronoamperometry plot for the ring electrode held at a constant potential of 0.7V vs. Hg/HgO (1M KOH). The rotation per minute was 1600.

Calculation of Tafel slope

Tafel slope is calculated to evaluate the kinetics of electrochemical reaction activity of electrocatalysts. Tafel slope tells about the kinetics of the reaction and the one with lower tafel slope will be the best catalyst.

$$\text{Tafel equation, } \eta = b \log(j/j_0)$$

Where η is the overpotential, **b** is the Tafel slope and **j** is the current density and j_o is the exchange current density.

Figure 3.9 shows the Tafel plot for all catalyst and calculated Tafel slope are given in the Table 3. β-FeOOH @ α-Fe$_2$O$_3$ catalyst exhibit Tafel slope of 91mV/decade whereas β-FeOOH nano and rod α-Fe$_2$O$_3$ nano cube shows a higher value 150mV/decade and 218mV/decade respectively. The observed Tafel slope value suggest that the β-FeOOH @ α-Fe$_2$O$_3$ hybrid is better catalyst for OER. Since the Tafel slope value for α-Fe$_2$O$_3$ is high it shows least activity towards OER. These observations are matching with voltammetric analysis of these catalysts. This again proves the superior OER activity of FeOOH @ α-Fe$_2$O$_3$ hybrid sample.
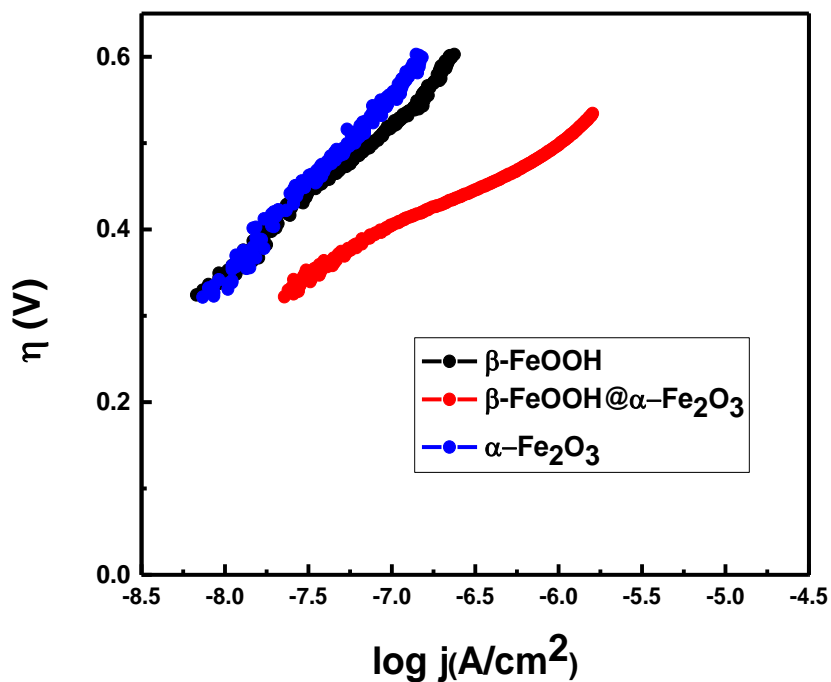
Figure.3.9: Tafel curves of β-FeOOH, β-FeOOH @ α-Fe$_2$O$_3$ andα-Fe$_2$O$_3$ electrocatalysts in 1M KOH

Table 3. Tafel slope for electrocatalyst.

Catalyst	β-FeOOH nano rod	β-FeOOH @ α-Fe$_2$O$_3$	α-Fe$_2$O$_3$ nano cube
Tafel slope(mV/decade)	150	91	218

3.4.2. Catalytic activity towards Oxygen Reduction Reaction

We conducted linear sweep voltametry (LSV) of α-Fe$_2$O$_3$ nanocubes, β-FeOOH nanotube and mixed phase α-Fe$_2$O$_3$@ β-FeOOH to evaluate the electrocatalytic activity towards ORR. Figure 3.10(a, b, c) shows the LSV of above three samples in N$_2$ and O$_2$ saturated 1M KOH solution.

Measurement in O_2 saturated and N_2 saturated solution confirm the ORR catalytic activity of the sample.

Due to the absence of oxygen in N_2 saturated electrochemical cell the samples showed very less activity towards oxygen reduction reaction. As shown in Figure 3.10(d) the onset potential for α-Fe_2O_3 nanorods occurred at 0.7V vs. RHE. The other two samples showed almost similar onset potential value, which approximately 0.6 V vs RHE. This suggests that the α-Fe_2O_3 nanocube is a better ORR electrocatalyst compared to the β-FeOOH nanorod and β-FeOOH@α-Fe_2O_3 phase.

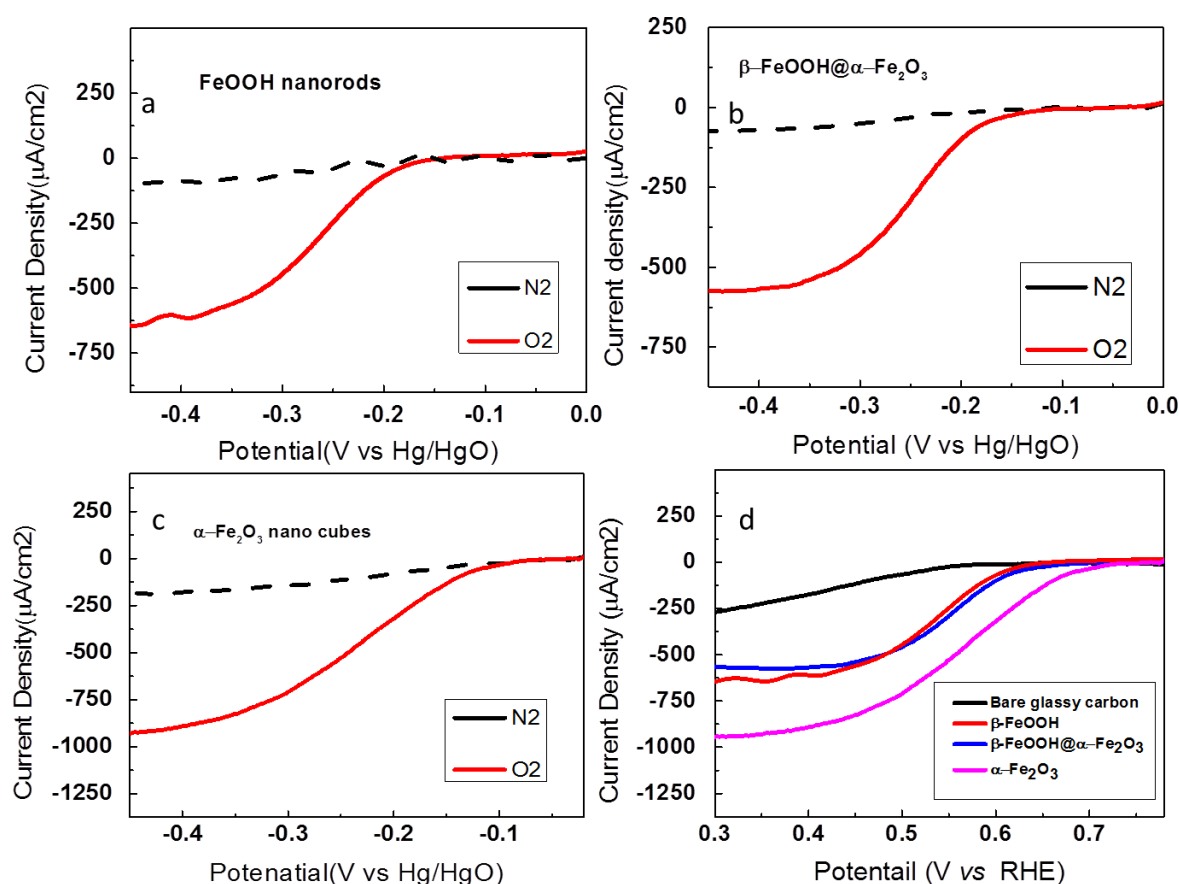
Figure 3.10: ORR activity of (a) β-FeOOH nanorods (b) β-FeOOH/α-Fe_2O_3 mixed phase and (c) α-Fe_2O_3 in N_2 (dotted line) and O_2 (solid line) atmosphere: (d) ORR activity of all three sample compared to bare glassy carbon electrode.

From the comparative electrocatalytic study of OER and ORR for three different samples, it is found that β-FeOOH@α-Fe$_2$O$_3$ is a better catalyst for OER and α-Fe$_2$O$_3$ possessed better activity towards ORR. By controlling the synthetic parameters we are able to tune the interfacial activity of transition metal oxides with selective activity towards OER and ORR.

3.5. Zinc Air battery

Since α-Fe$_2$O$_3$ possessed decent ORR activity and β-FeOOH/α-Fe$_2$O$_3$ hybrid phase possessed better OER activity we attempted them as electrocatalysts to construct rechargeable metal-air batteries. Figure 3.11(a) shows the polarization curve of a Zinc air battery with α-Fe$_2$O$_3$ as the cathode electrocatalyst in the presence (blue line) and absence of (red) oxygen. Polarization curve without oxygen demonstrated lower current density value compared with oxygen purging. This confirms the oxygen reduction activity of α-Fe$_2$O$_3$. The Zn-air battery showed a maximum power density of ~ 30mW/cm^2 at a current density ~ 35 mA/cm^2 (Figure 3.11(a)). Galvanostatic polarization at a current density of 10 mA/cm^2 demonstrated a discharge capacity (normalized to consumed Zn weight) of ~580 mAh/g (Figure 3.11(b)) with α-Fe$_2$O$_3$ electrocatalyst. However when α-Fe$_2$O$_3$ alone was employed as the cathode catalyst in Zn-air batteries, the resulting charging overpotential was significantly higher and therefore the battery was mainly primary in nature, Figure 3.12(a). The introduction of β-FeOOH@ α-Fe$_2$O$_3$ phase to Zn-air battery in a trielectrode configuration resulted in ~500 mV reduction in overpotentials during the charge chemistry, leading to a rechargeable Zn-air battery with extended cyclability (Figure 3.12(a) and Figure 3.12(b)). This again demonstrates that by tuning the synthetic parameters the interfacial activity of transition metal oxides can be tuned by selective imparting of ORR or OER.
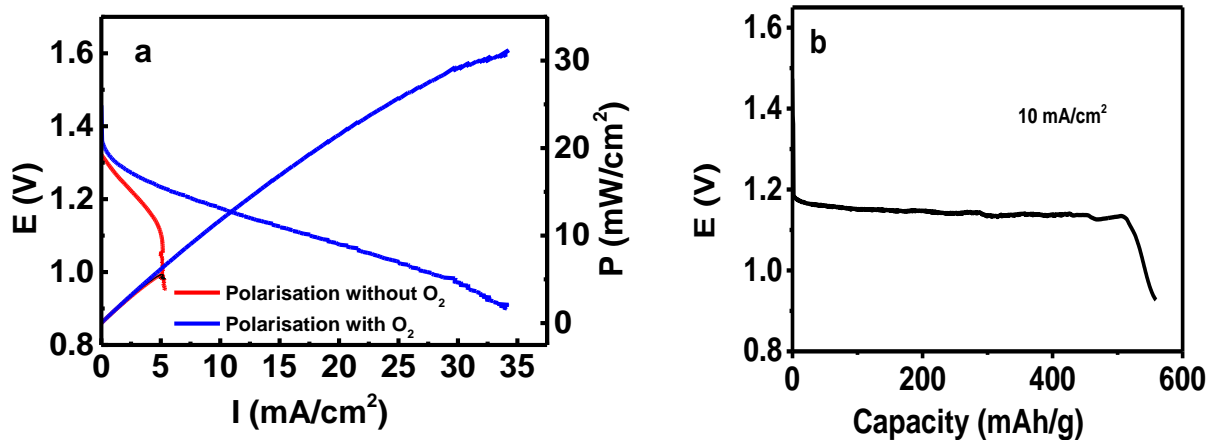
Figure 3.11: (a) Zinc-air battery polarisation with and without O$_2$ purged in 6 M NaOH with α-Fe$_2$O$_3$ ORR catalyst and b) the corresponding galvanostatic discharge curve at a current density of 10 mA/cm2.
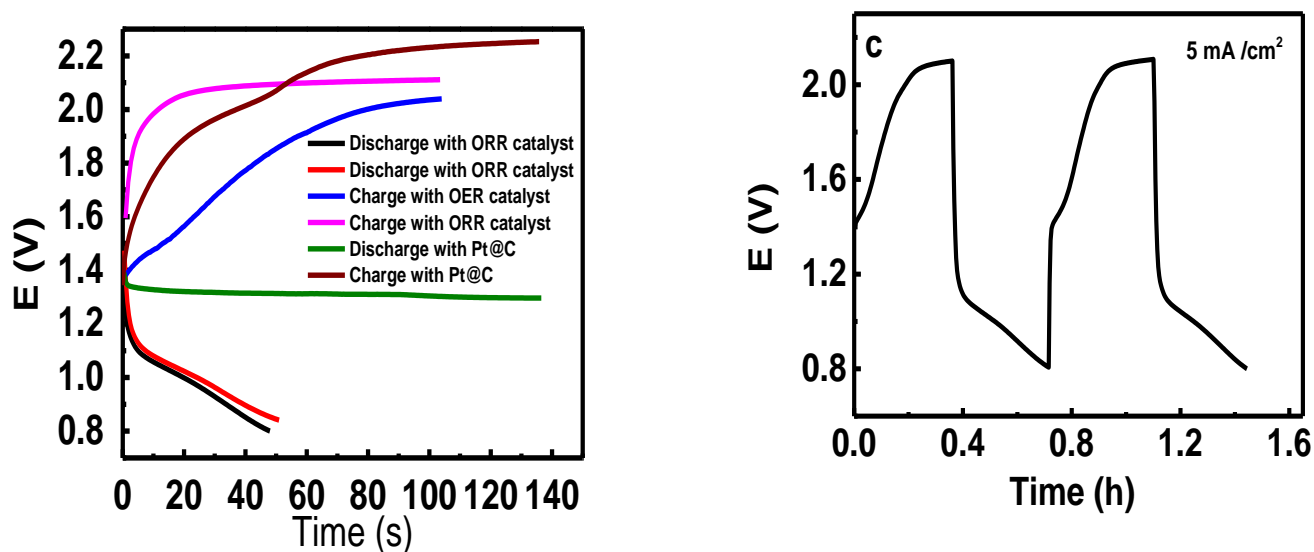
Figure 3.12: (a) Zn-air battery performance metrics with only α-Fe$_2$O$_3$ ORR catalyst, with α-Fe$_2$O$_3$ ORR catalyst and OER catalyst in trielectrode configuration and Pt@C state of the art air cathode at 5 mA/cm^2 current density.(b) Zinc-air rechargeable battery with a tri-

electrode configuration in 6M NaOH. Charging was carried out with OER catalyst and discharging was done with ORR catalyst.

Zn-air battery performance with state of the art air cathode Pt@C is provided in Figure 3.12a. The supremacy of Pt compared to α-Fe_2O_3 as an ORR catalyst is evident in Zn-air battery performance curves, Figure 3.12a. However a comprison of charging curves with β-$FeOOH$@α-Fe_2O_3 and Pt deomnstrate the advantage of adopted synthetic stategy with a noticeable reduction in charging voltage in the former compared to the latter. This indicate that eventhough the synthetic strategy presented here is able to tune the interfacial chemistry of iron oxides, their activity towards ORR should be definitely improved to design a competing electrocatalyst to Pt. This can be achieved by designing hybrid materails with graphene, carbon nanotubes etc. and it will be a matter of future investigation.

Conclusion

In present investigation, we synthezised hamatite nanocubes by template free one - pot hydrothemal method. It is observed that the intermediate β- FeOOH phase undergoes morphological and nanostructured phase transformation to α-Fe$_2$O$_3$ naocrystals. The oxyhydroxide β-FeOOH phase, act as a template for the formation of the hematite nanocrystals. The size, shape and morphology of the nanocrystals are largely governed on the reaction conditions and we could see interesting phase evolutions with different sizes and shape of the nanocrystals by changing the hydrothermal treatment time of the reaction mixture and the supersaturation levels of the reaction mixture. For the selected shape of the hematite nanocubes an exceptionally high coercivity of ~ 5.3 kOe is observed confirming presence of strong ferromagnetism. Comparitive electrocatalytic study was conducted for oxygen evolution and oxygen reduction reactions. β-FeOOH@α-Fe$_2$O$_3$ shows superior OER activity with a current density of 10mA/cm^2 at an overpotential of 1.78V vs RHE.α-Fe$_2$O$_3$ shows better ORR activity compared to other samples. We investigated β- FeOOH@α-Fe$_2$O$_3$ and α-Fe$_2$O$_3$ as OER and ORR electrocatalyst in rechargeable zinc- air battery. Indeed more work has to be done in this area in order to increase the efficiency of ORR catalyst to design a competing alternate to state of the art Pt@C air electrode.

Future Prospects

As we can systematically control the shape, size and morphology of the hematite nanocrystals, it is interesting to study the photochemical degradation of organic dyes for the purification of water. Work in this direction is in progress. More work in the area of zinc air battery is planned in order to increase its current density and power density.

Reference

1. Hu,S.Y.; Schwarsctein,K.A.; Forman,J.A.; Hzen,D.; Park,J.N.;McFarland,E.W. *Chem. Mater.***2008**, *20* (12), 3803–3805.

2. Wu,Z.; Yu,K.; Zhang,S.; Xie,Y. *J. Phys. Chem. C.* **2008**, *112* (30), 11307–11313.

3. K.Townsend,T.; M.Sabio,E.; Browing,Nigel.;Osterloh, F.*Energy Environ. Sci.***2011**, 4, 4270

4. Liu, D.; Li, Z.; Wang,W.; Wang,G.;Liu,D. *J. Alloys and Compds.* **2016** *654*, 491-497.

5. Wu, W.; Zhang,S.; Xiao,X.; Zhou,J.; Ren,F.; Sun,L.; Jiang,C. *ACS Appl. Mater. Interfaces.***2012**, *4*, 3602−3609.

6. Kang,J.; Kuang,Q.; Xie,Z.X.; Zheng,L.S. *J. Phys. Chem. C.***2011**,*115*,7874–7879.

7. Wang,L.; Wei,H.; Fan,Y.; Gu,X.; Zhan,J. *J. Phys. Chem. C.***2009**,*113*,14119–14125.

8. Steele,B.C.H.; Heinzel,A. *Nature.2001,* 414, 345-352.

9. Kanan,M.;Nocera,D. *Science.***2008,**321, 1072-1075.

10. McDaniel,N.; Coughlin,F.; Tinker,L.; Bernhard,*J. Am. Chem. Soc.* **2008**,*130*, 210–217.

11. Schulze,M.; Kunz,V.; frischmann,P.; Wunrthner,F. *Nature Chemistry.* **2016,** *8*, 576-583.

12. Fillol,J.; Codola,Z.; Bosch,L.; PLa,J.; Costas,M. *Nature Chemistry.* **2011,** *3*, 807-813.

13. Jiao,F.; Frei,H. *Energy Environ. Sci.* **2010**, 3, 1018–1027.

14. Wang,D.; Chen,X.; Evans,D.; Yang,W. *Nanoscale.* **2013**, 5, 5312.

15. Singh,R.N.; Lal,B. *International Journal of Hydrogen Energy.***2002**, 27, 45-55

16. Zhao,Y.; Chen,S.; Sun,B.; Su,D.; Haung,X.; Yan,Y.; Sun,K.; Wang,G. *Scientific Report.* **2015**,*5*,762*.*

17. Greeley,J.; Stephen,I.E.L.; Bondarenko,A.S.; Johansoon,T.P.; Hansen,H.A.; Jaramillo,T.F.; Rossmeisl,J.; Chorkendoff,I.; Norskov,J.K. *Nature Chemistry .***2009**,*1*,552-556.

18. Wang.B. *Journal of Power Sources.***2005**,152,1-15.

19. Sun,M.; Zhang,G.; Lui,H.; Liu,Y.; Li,J. *Sci China Mater .***2015**, 58, 683–692.

20. Jang,B.; Bong,S.; Woo,S.; Park,S.;Ha,J.; Choi,E.; Piao,Y. *J. Nanosci. Nanotechnol.***2014***,* 14, 8852–8857.

21. Lee,J.; Kim,S.; Cao,R.; Choi,N.; Liu,M.; Lee,K.; Cho,J. *Adv. Energy Mater.* **2011,** 1,34-50.

22. Linden,D.; Reddy,B.T**.***Handbook of batteries,*3rd edition, Mc Graw-hill publication.

23. Li,Y.' Gong,M.; Liang,Y.; Feng,J.; Kim,J.; Wang,H.; Hong,G.; Zhang,B.;Dai,H. *Nature Communications.***2013**,4,1-7.

24. Chen,Z.; yu,A.; Ahmed,R.; Wang,H.; Li,H.; Chen,Z. *Electrochimica Acta .***2012**, *69*,295–300.

25. Yaun,L.; Wang,J.; Jiang,Q.; Zhou,G. *J. Mater. Res.***2012,** 27,1014-1021.

26. Wu,C.; Yin,P.;Zhu,X.; Yang,C.; Xie,Y. *J. Phys. Chem. B.* **2006**,110,17806-17812.

27. Suresh,R.; Prabhu,R.; Vijayaraj,A.; Giribabu,K.; Stephen,A.; Narayanan,V.; *Materials Chemistry and Physics.***2012**,134,590-596.

28. Wang,S.; Min,Yu.; Yu,Shu.; *J. Phys. Chem. C.* **2007,**111,3551-3554.

29. Kandori,K.; Sakai,J.; Ishikawa,T. *Phys. Chem. Chem. Phys.* **2000**, 2,3293-3299.

30. Wang,C.; Shi,J.; Cui,X.; Wang,H.; Wu,J.; Zhang,C.; Wang,L.; Xu,Y. *J. Mater. Chem. A,* **2016**, 4, 11000–11008.

31. *Elements of X-ray Diffraction*, ed. by B. D. Cullity ,Addison Wesley Publishing.**1978** .

32. C. N. Banwell, E. M. McCash, A Book: *Fundamentals of Molecular Spectroscopy* 4th Ed. Tata McGraw Hill Publishing Co. Ltd., **2002.**

33. championed.info/schematic/schematic-of-spectrophotometer.html

34. Remazeilles,C.; Refait,P. *Corrosion Science.* **2007**, *49* 844–857.

35. He,Y.P.; Miao,M.Y.; Li,C.R.; Wang,S.Q.; Cao,L.; Xie,S.S.; Yang,G.Z.; Zou,S.B. *Phys. Rev. B.* **2005**,71,12541.

36. Weber, M. F.; Dignam, M. J. J. *Electrochem. Soc.* **1984**, *131*,1258-1265.

37. Gorlin, Y.; Jaramillo, T. F. *J. Am. Chem. Soc.* **2010**, *132*, 13612-13614.

38. McCrory,C.L.C.; Jung,S.; Peters,C.J.;Jaramillo,F.T. *J. Am. Chem. Soc.* **2013**, 135, 16977-16987.